American Journal of Aerospace Engineering
2026, Vol. 12, No. 2, pp. 40–52
https://doi.org/10.11648/j.ajae.20261202.12

Research Article

Transonic Flow Past Wing Optimised for Supersonic Flow with Pitching Moment Constraint

Maddineni Sai Deekshit*, **Satish Chander Gupta**

Department of Aeronautical Engineering, MVJ College of Engineering, Bengaluru, India

Abstract

In high-speed aerodynamic design, wings optimized for supersonic cruise often experience a severe rearward migration of the aerodynamic center upon transitioning from transonic to supersonic regimes. This Mach tuck phenomenon enlarges vehicle static margins, diminishes pitch control authority, and imposes substantial trim drag penalties. To address this trade-off, this study investigates the aerodynamic optimization of a candidate low-aspect-ratio delta wing (AR = 2.9, Λle = 50°, λ = 0.1417) at a supersonic design point (M∞ = 1.1, α = 2°) subject to an explicit pitching-moment constraint, followed by an evaluation of off-design transonic flow behavior. A numerical framework based on the method of undetermined Lagrange multipliers is applied to closed-form constant-pressure vortex panels to minimize induced drag while enforcing target lift and pitching-moment values. The resulting optimal warp is decoupled into spanwise washout (twist) and chordwise camber slopes, which are subsequently superimposed onto a baseline NACA 0006 thin airfoil. Transonic flow analysis is performed across Mach numbers M∞ = 0.90–0.95 using a three-dimensional transonic small perturbation (TSP) formulation solved via finite-difference line relaxation with Murman-Cole type shock-capturing artificial viscosity. The results reveal that constraining pitching moment by 10% (0.9M̄y) shifts the aerodynamic center forward from 75.4% cr to 66.8% cr, mitigating Mach tuck while simultaneously reducing the wing-root bending moment by 3.18%. This stability benefit is achieved with a 26.30% reduction in induced drag relative to the flat plate (CDi = 0.0042 vs 0.0057), incurring a modest 9.5% drag increment compared to the unconstrained-moment optimum (CDi = 0.0038). Geometric decoupling demonstrates that the required moment relief is accommodated predominantly by localized reflex camber near the root, while camber increases progressively outboard toward the tip. Off-design transonic evaluations capture upper-surface shock wave formation that intensifies toward the wing tips. These findings demonstrate that tailoring supersonic camber with a pitching-moment constraint effectively balances supersonic trim stability against off-design transonic aerodynamic performance.

Keywords

Transonic Flow, Supersonic Wing Optimization, Pitching-moment Constraint, Induced Drag Minimization, Transonic Small Perturbation Equation, Aerodynamic Center Shift, Reflex Camber

*Correspondence: Maddineni Sai Deekshit (deekshu674@gmail.com)

Received: 24 October 2026; **Accepted:** 12 November 2026; **Published:** 27 November 2026

Copyright: © The Author(s), 2026. Published by Science Publishing Group. This is an **Open Access** article, distributed under the terms of the Creative Commons Attribution 4.0 License (http://creativecommons.org/licenses/by/4.0/), which permits unrestricted use, distribution and reproduction in any medium, provided the original work is properly cited.

1. Introduction

Transonic flow represents one of the classical and most enduring challenges in fluid dynamics and aerospace engineering [1, 10, 11]. In the transonic regime, regions of embedded supersonic flow co-exist with subsonic freestream flow, yielding a mixed elliptic-hyperbolic system governed by non-linear potential or Euler equations [8, 10]. The local deceleration from supersonic pockets back to subsonic conditions typically occurs across compression shock waves formed on the wing upper surface [9, 16]. These shock waves induce steep adverse pressure gradients, boundary-layer thickening or separation, buffet instabilities, and a drastic rise in wave drag [13, 16]. Consequently, designing aerodynamic surfaces that maintain high efficiency across both transonic and supersonic regimes remains an essential aerodynamic requirement [1, 15].

For high-speed aircraft and fighter configurations operating across multiple speed regimes, this fluid-dynamic complexity is compounded by longitudinal stability and trim characteristics [2, 4, 14]. During the transition from transonic to supersonic flight, the aerodynamic center of the wing experiences a pronounced rearward migration—a flight mechanics phenomenon known as 'Mach tuck' [2, 14]. This rearward shift significantly inflates the vehicle's static margin. While increased static margin enhances longitudinal static stability, it severely impairs pitch control authority and demands substantial trailing-edge elevon deflections to trim the aircraft [4, 14]. The resulting trim drag can compromise the operational range and aerodynamic performance of supersonic designs [6, 14, 15].

To resolve this conflict, aerodynamic shape optimization (ASO) frameworks have increasingly sought to integrate stability and trim constraints into drag minimization workflows [1, 4, 14]. While classical supersonic camber design techniques [2, 12] and modern gradient-based adjoint formulations [1, 13] have successfully minimized induced or wave drag at a single supersonic cruise condition, designs optimized without longitudinal moment constraints often exhibit undesirable trim penalties or adverse off-design characteristics [4, 14]. Moreover, although supersonic vortex panel methods provide exact gradient information for rapid camber optimization [2, 3, 5], the off-design transonic behavior of wings shaped by such constrained supersonic camber distributions has not been adequately explored.

A critical research gap exists in understanding how enforcing an explicit supersonic pitching-moment constraint reshapes the spanwise and chordwise camber distributions, and how the resulting cambered wing performs in off-design transonic flight where non-linear shock waves emerge. Specifically, questions remain regarding how localized geometric features—such as root reflex camber and spanwise washout—influence the strength, location, and three-dimensional development of upper-surface shock waves under transonic flow conditions.

To address this gap, the present study develops an integrated computational investigation. First, a low-aspect-ratio delta wing representative of high-speed fighter aircraft is optimized at a low supersonic Mach number ($M\infty = 1.1$, $\alpha = 2°$) for minimum induced drag subject to specified lift and pitching-moment constraints using the method of undetermined Lagrange multipliers applied to constant-pressure vortex panels [2, 3]. Second, the optimal aerodynamic warp is decoupled into spanwise washout (twist) and chordwise camber slopes, which are superimposed onto a thin baseline aerofoil (NACA 0006). Third, the resulting three-dimensional wing geometry is analyzed under transonic flow conditions ($M\infty = 0.90–0.95$) and higher supersonic regimes ($M\infty = 1.55–2.0$) using a finite-difference formulation of the 3D Transonic Small Perturbation (TSP) equation equipped with Murman-Cole type shock-capturing artificial viscosity [8, 10]. This work establishes how a 10% pitching-moment constraint alters structural bending moments, aerodynamic center locations, and off-design transonic shock behavior without compromising the underlying aerodynamic efficiency.

2. Mathematical Formulation

2.1. Wing Discretization and Supersonic Vortex Panel Method

To critically contextualize the present methodology and findings, existing research is organized around four key themes:

Transonic Aerodynamics and Numerical Potential Flow Methods: Foundational numerical schemes for transonic flows were established by Murman and Cole [10], who introduced type-dependent finite-difference operators for the transonic small perturbation equation, applying central differencing in elliptic (subsonic) zones and backward upwind differencing in hyperbolic (supersonic) zones. Steger and Klineberg [8] extended finite-difference relaxation techniques to transonic airfoil design, while Jameson [11] generalized iterative potential flow methods to 3D transonic wings. More recently, Premasuthan et al. [9] developed spectral difference schemes incorporating artificial viscosity for robust shock capturing, and Petrocchi et al. [16] investigated transonic shock buffet alleviation via virtual control surfaces. These studies confirm that potential-based finite-difference formulations capture the essential physics of transonic shock waves and surface pressure distributions with high computational efficiency.

Supersonic Wing Optimization and Induced Drag Minimization: Classical linear supersonic theory established that wing warp (combined twist and camber) can substantially reduce induced and wave drag [2, 12]. Carlson and Miller [12] and Sorrells and Miller [2] developed vortex-panel methodologies for minimum-drag supersonic camber design under moment and deformation constraints. Modern aerodynamic shape optimization has expanded into high-fidelity adjoint

formulations [1, 14]. As surveyed by Martins [1], adjoint methods provide gradient evaluations whose computational cost is independent of design variables. Malone and Mason [6] coupled analytic technology models for multidisciplinary aircraft optimization. In related work, Gupta [3, 5, 7] developed algorithmic frameworks and reconstructive approaches for planar supercritical and optimized wings, demonstrating the utility of exact gradient formulations in preliminary aerodynamic design.

Pitching-Moment Constraints and Longitudinal Stability Management: Incorporating stability constraints into aerodynamic optimization is essential for realistic aircraft configurations. Mader and Martins [4] showed that unconstrained drag minimization of flying-wing configurations yields aerodynamically efficient profiles that are statically unstable, whereas enforcing static stability constraints drives distinct planform sweep and reflex camber adaptations. Seraj et al. [14] conducted RANS-based aerodynamic shape optimization of a supersonic transport under subsonic static margin constraints, proving that enforcing low-speed pitch stability incurs a measurable supersonic cruise drag penalty. Chau and Zingg [15] highlighted the necessity of multipoint optimization to avoid performance degradation at off-design conditions, while Pang et al. [17] and Sudhi et al. [18] developed advanced geometric parameterization techniques to ensure smooth transonic and supersonic airfoil deformations under multi-objective constraints.

Synthesis and Research Gap: While existing literature encompasses both supersonic camber optimization and transonic flow analysis, they have predominantly been treated in isolation. Studies optimizing supersonic wings with pitching-moment constraints [2, 4, 14] have seldom examined the detailed three-dimensional transonic flowfield and shock structures that arise when those optimized geometries cruise or maneuver at transonic speeds. The present paper directly links supersonic panel-based camber optimization under an explicit 10% pitching-moment constraint with detailed 3D transonic small perturbation analysis, uncovering the localized mechanisms of root reflex camber and spanwise shock intensification.

2.2 Optimisation Formulation

In the approach made here, wing is represented by a large number of closed forms of constant pressure panels to model circulation. Chordwise paneling is taken for geometry discretization. Figure 1 shows axis system and related moments and paneling scheme with Mach wave and upstream Mach cone. These panels are used for estimation of pressure difference coefficients. The circulation is determined through tangential flow boundary conditions and pressure difference coefficient is given by $\Delta Cp = 2\gamma/U$. Downwash for satisfying tangential flow boundary conditions at collocation points are determined from region within upstream Mach cone originating from collocation points. Collocation points are located at 95% of local panel chords where Neumann boundary conditions are applied. Lift is determined through integration of ΔCp over the chord and span. Thereafter optimization constraints are taken into consideration. Initially a flat surface is considered and due to the effort of optimization, the initial flat wing becomes cambered and creates washout. Objective function (F) for the drag minima and specified value of lift ($\bar{L}$) is first written in Lagrange form using Lagrange multiplier λ_0 as below:

$$F = D + \lambda_0(L - \bar{L}) \tag{1}$$

Lift is obtained from the following expression:

$$L = \rho U[A_1\gamma_1 + \cdots + A_N\gamma_N] \tag{2}$$

here, $\gamma_1,\ldots\ldots\gamma_N$ are circulation strength of N number of panels & $A_1,..A_N$ are related panel areas. Objective function (F) is differentiated w.r.t circulation and Lagrange multiplier as below:

$$\frac{\partial F}{\partial \gamma_k} = 0, \text{ for k= 1, 2, N and } \frac{\partial F}{\partial \lambda_0} = 0 \tag{3}$$

This results in Eq. (4).

$$\begin{bmatrix} 2A_1a_{1,1} & . & . & . & (A_1a_{1,N} + A_Na_{N,1}) & A_1 \\ . & & & & . & . \\ . & & & & . & . \\ . & & & & . & . \\ (A_Na_{N,1} + A_1a_{1,N}) & . & . & . & 2A_Na_{N,N} & A_N \\ A_1 & . & . & . & A_N & 0 \end{bmatrix} \times \begin{bmatrix} \gamma_1 \\ . \\ . \\ . \\ \gamma_N \\ \lambda_0 \end{bmatrix} = \begin{bmatrix} 0 \\ . \\ . \\ . \\ 0 \\ \bar{L} \end{bmatrix} \tag{4}$$

Circulation (γ) through this matrix gives optimum solution for minimum induced drag which is given by the following expression:

$$D_{\min} = \rho U \begin{bmatrix} \left(a_{1,1}\gamma_1 + \ldots + a_{1,N}\gamma_N\right)\gamma_1 A_1 + (a_{2,1}\gamma_1 + \ldots. + a_{2,N}\gamma_N)\gamma_2 A_2 \\ +\ldots\ldots\ldots\ldots\ldots + (a_{N,1}\gamma_1 + \ldots. + a_{N,N}\gamma_N)\gamma_N A_N \end{bmatrix} \tag{5}$$

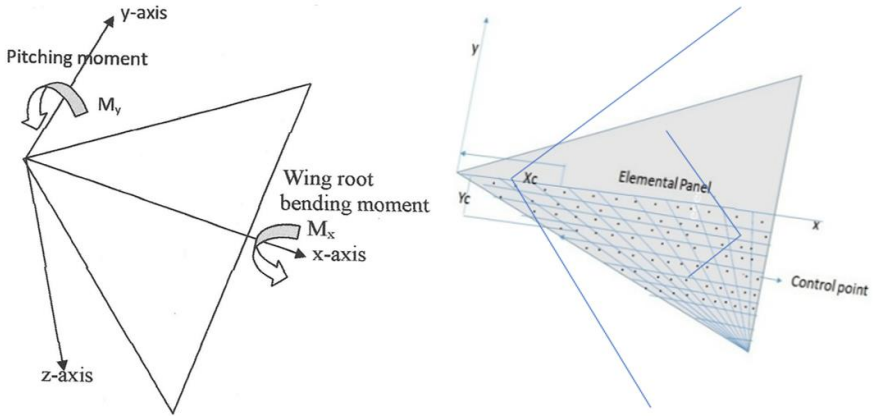

Figure 1. *Axis system and related moments and paneling scheme shown with Mach wave and upstream Mach cone.*

Once the circulation is found, the optimal camber ($dz/dx = ZX_i$) to support the minimum drag producing lift is determined from Eqn. (6).

$$ZX_i = (a_{i,1}\gamma_1 + \cdots + a_{i,n}\gamma_n)A_i \tag{6}$$

Likewise, in all a total of three different constraints are considered as given at Table 1.

Table 1. *Three Different Constraints.*

Constraint number	Constraint	Corresponding objective function
1	Lift	$F = D + \lambda_0(L - \bar{L})$
2	Lift and pitching moment	$F = D + \lambda_0(L - \bar{L}) + \lambda_1(M_y -)$
3	Lift and constrained pitching moment	$F = D + \lambda_0(L - \bar{L}) + \lambda_1(M_y - 0.9 * \bar{M}_y)$

For example, the objective function for 2nd constraint is written as below, where $\bar{L}, \bar{M}_y$ are specified value of lift and pitching moment.

$$F = D + \lambda_0(L - \bar{L}) + \lambda_1(M_y - \bar{M}_y) \tag{7}$$

Taking derivatives w.r.t. circulation and Lagrange results in following:

$$\begin{bmatrix} 2A_1a_{1,1} & \cdots & (A_1a_{1,N} + A_Na_{N,1}) & A_1 & A_1XC_1 \\ \vdots & & \vdots & \vdots & \vdots \\ (A_Na_{N,1} + A_1a_{1,N}) & \cdots & 2A_Na_{N,N} & A_N & A_NXC_N \\ A_1 & \cdots & A_N & 0 & 0 \\ A_1XC_1 & \cdots & A_NXC_N & 0 & 0 \end{bmatrix} \times \begin{bmatrix} \gamma_1 \\ \vdots \\ \gamma_N \\ \lambda_0 \\ \lambda_1 \end{bmatrix} = \begin{bmatrix} 0 \\ \vdots \\ 0 \\ \bar{L} \\ \bar{M}_y \end{bmatrix} \tag{8}$$

where $XC_1, \ldots XC_N$ are distances of panel control points from y-axis and $a_{i,j}$ are influence coefficient towards downwash velocities. Panel control points are collocation points that are located at 95% of local panel chords where Neumann boundary conditions i.e. the fluid velocity perpendicular to the surface is zero are applied. The solution of this matrix for specified values of $\bar{L}$ & $\bar{M}_y$ results in optimal circulation from where pressure difference coefficient, lift, drag, and pitching moment and wing root bending moments are determined.

Transonic flow is progressed to study the effect of drag rise

in transonic regime. Transonic small perturbation equation below is used, where $\Re$ is the ratio of specific heats [7-9].

$$\left[\left(1-M^2\right)\phi_x\right]_x+\phi_{yy}+\phi_{zz}=0 \tag{9}$$

where $1-M^2=1-M_\infty^2-K\,\phi_x$ and $K=\frac{2}{U}[1+\frac{\Re-1}{2}M_\infty^2]M_\infty^2$

Equation (9) is solved with finite difference methodology with line relaxation process. The computational plane from the geometric plane is developed in the following manner.

$$\xi=\frac{x-x_{1e}}{x_{te}-x_{le}},\ \eta=y,\ \zeta=z \tag{10}$$

Using this transformation, the values of ϕ derivatives become as:

$$\phi_x=\phi_\xi\,\xi_x$$

$$\phi_y=\phi_\xi\,\xi_y+\phi_\eta$$

$$\phi_z=\phi_\zeta$$

$$\varphi_{xx}=\left(\varphi_\xi\ \xi_x\right)_\xi\ \xi_x$$

$$\varphi_{yy}=\left(\varphi_\xi\ \xi_y+\varphi_\eta\right)_\xi\ \xi_y+\left(\varphi_\xi\ \xi_y+\varphi_\eta\right)_\eta$$

$$\varphi_{zz}=\phi_{\xi\xi}$$

Using these above equations, transonic small perturbation equation is written as below:

$$\left(1-M^2\right)\left(\phi_\xi\,\xi_x\right)_\xi+\frac{\xi_y}{\xi_x}\left(\phi_\xi\,\xi_y+\phi_\eta\right)_\xi+\frac{1}{\xi_x}\left(\phi_\xi\,\xi_y+\phi_\eta\right)_\eta+\frac{1}{\xi_x}\phi_{\zeta\zeta}=0 \tag{11}$$

with $\xi_x=1/c$, and $\xi_y=\tan\wedge/c$ or

$$\left[\left(1-M^2\right)\ \xi_x^2+\xi_y^2\right]\ \varphi_{\xi\xi}+\xi_y\left(\varphi_{\eta\xi}+\varphi_{\xi\eta}\right)+\varphi_{\eta\eta}+\varphi_{\varsigma\varsigma}=0 \tag{12}$$

Condition for elliptic region for equations (11) or (12) is $\left[\left(1-M^2\right)\ \xi_x^2+\xi_y^2\right]>0$, and Condition for hyperbolic region is $\left[\left(1-M^2\right)\ \xi_x^2+\xi_y^2\right]<0$

In case of elliptic form of equation, the normal component of freestream Mach number perpendicular to leading edge is less then unity. The derivatives of φ are determinable through chain rue relationship between two coordinate systems. Vertical derivative is used to satisfy tangential flow boundary condition. When equation is in elliptic form, central difference operator is used, and when it is in hyperbolic form then upwind bias though backward difference is applied. The change of this operator results in capturing shock waves. Switching to an upwind scheme from central difference aligns the numerical math with physical reality. It allows numerical perturbations to propagate only along the physical characteristic lines. This creates a smooth, physically accurate Mach wave. Switching from upwind back to a central scheme introduces downstream information into a zone that should only care about upstream conditions. This violates the hyperbolic nature of supersonic flow equations. The scheme tries to capture an unphysical upstream propagation of data, forcing the flow to sharply discontinue. In physical modeling, this sudden, non-linear compression manifests as a sharp shock wave to match the pressure and velocity jumps. Such a shock captured in a potential flow using unwinding is not adiabatic; instead, it behaves as an isentropic compression. It is for this reason that a lower Mach number of 1.1 value is taken in supersonic regime for this work.

Switching scheme is essentially a subtraction of artificial viscosity i.e $\Delta\xi\,(M^2-1)\,\varphi_{\xi\xi\xi}$ while turning into upwind scheme from central difference scheme, and an addition of this term while turning into central difference scheme from rearward scheme. It appears that as $M^2\to 1$, the term representing artificial viscosity goes to a near zero value and is doing compression to grid width if multiplied with $\Delta\xi$, but this is not the case. The term typically emerges as a third-order dispersion error (which acts to counter numerical oscillations) from the modified equation analysis of numerical schemes used for potential flow equations such as the current schemes for the transonic small perturbation equation. It modifies the magnitude of a truncation error term by changing the numerical resolution of a gradient, but it does not compress the grid.

3. Results and Discussions

Wing of following dimension is considered as candidate for a fighter role application.

Leading edge sweep $=50^0$
Trailing edge sweep $=12.7^0$
Taper ratio $=0.1417$
Aspect ratio $=2.9$

Cr=7.41m
Ct=1.05
b=12.5m

Flat surface wing is taken to start the optimisation process. Freestream Mach number is taken as 1.1, and angle-of-attack is taken as 2^0. Low supersonic Mach number is taken to keep leading edge largely subsonic. Table 2 shows the values of lift coefficient, induced drag coefficient, moment coefficients as ratios of values before and after optimisation. First and second constraint show almost same values. The 3rd constraint is introduced by reducing the pitching moment by 10% of value obtained in this constraint before optimisation. Comparing 1st and 3rd constraints, there is increase in drag by 9.5% and reduction in wing root bending moment by 3.18%. Aerodynamic centre is determined and seen to move forward to 66.8% from 75.4% on root chord.

Table 2. *Aerodynamic coefficients derived for minimum induced drag for varied constraints, M∞ = 1.1, α = 2°.*

Constraint Number	Constraint parameter	Before Optimisation C_L	After Optimisation C_L^*	C_L^*/C_L	C_{Di}		Drag reduction	C_L/C_{Di}		Cm_y^*/Cm_y	Cm_x^*/Cm_x
					Before	After	%	Before	After		
1	L	0.1627	0.1627	1.0	0.0057	0.0038	33.33	28.54	42.81	1.0217	0.9569
2	L, My	0.1627	0.1627	1.0	0.0057	0.0038	33.33	28.54	42.81	1.0	0.9518
3	L, 0.9My	0.1627	0.1627	1.0	0.0057	0.0042	26.30	28.54	38.74	0.9	0.9264

Note: Asterisk mark (*) indicates values after optimisation. Constraints 1 and 2 show no noticeable differences. Under Constraint 3, the wing-root bending moment is reduced by 3.18%, and the aerodynamic center shifts forward to 66.8% from 75.4% root chord, at the cost of a 9.5% induced drag increase relative to Constraint 1.

The quantitative comparisons summarized in Table 2 elucidate the fundamental trade-offs between drag minimization and longitudinal stability constraints. For Constraint 1 (lift constraint only), the induced drag coefficient is reduced by 33.33% from CDi = 0.0057 to 0.0038, boosting the lift-to-induced-drag ratio CL/CDi from 28.54 to 42.81. The pitching moment ratio My*/My remains essentially unchanged at 1.0217, while the wing-root bending moment ratio Mx*/Mx drops slightly to 0.9569. Constraint 2 (simultaneous lift and unconstrained pitching-moment constraint) exhibits virtually identical performance (CDi = 0.0038, My*/My = 1.0, Mx*/Mx = 0.9518). However, when a 10% pitching-moment reduction is enforced under Constraint 3 (L, 0.9My), significant aerodynamic and structural shifts occur. The aerodynamic center shifts forward from 75.4% cr to 66.8% cr, providing a substantial 8.6% root-chord forward shift that directly mitigates Mach tuck and alleviates the trim authority penalty. Concurrently, the wing-root bending moment ratio decreases to 0.9264—representing a 3.18% structural relief relative to Constraint 1—which is highly beneficial for reducing wing-root structural weight. This stability and structural relief is achieved while still delivering a 26.30% induced drag reduction relative to the flat plate (CDi = 0.0042 vs 0.0057), incurring a modest 9.5% drag trade-off compared to the unconstrained-moment optimum (CDi = 0.0038).

Figure 2 illustrates the chordwise pressure difference coefficient across the baseline flat plate surface at the root, mid-semispan, and tip stations. At the supersonic design condition of M∞ = 1.1, the Mach cone half-angle is μ = arcsin (1/1.1) = 65.38°. Consequently, the Mach wave originating from the wing apex lies 25.38° ahead of the wing leading edge (sweep angle Λle = 50°), rendering the leading edge aerodynamic behavior subsonic. Because the leading edge is subsonic, the flow field is no longer purely conical; fluid communication occurs between the upper and lower surfaces, generating an upwash along the leading edge. Conversely, the trailing edge is swept at Λte = 12.7°, which is 11.92° behind the Mach wave originating from the root trailing edge, establishing a supersonic trailing-edge flow regime. In this supersonic trailing-edge zone, flow disturbances cannot propagate upstream, and the classical Kutta condition is neither required nor applicable. Aerodynamic loading is carried continuously to the trailing edge.

Comparing the flat plate pressure distribution with the optimal camber profile generated under Constraint 1 (Figure 3), a pronounced rearward shift in peak loading is evident across all three spanwise stations. For the flat plate, high leading-edge suction rapidly decays toward the trailing edge. In contrast, the optimized camber distribution relieves the excessive leading-edge loading and redistributes lift across the mid-chord region. Because the trailing edge remains supersonic, finite positive loading is maintained all the way to the trailing edge. Multiplying the revised chordwise loading by the local moment arms preserves the net pitching moment (My*/My = 1.0217 as reported in Table 2). Given that Constraints 1 and 2 yield virtually identical aerodynamic polars, subsequent analyses focus on comparing the unconstrained-moment design (Constraint 1) with the pitching-moment-constrained design

(Constraint 3).

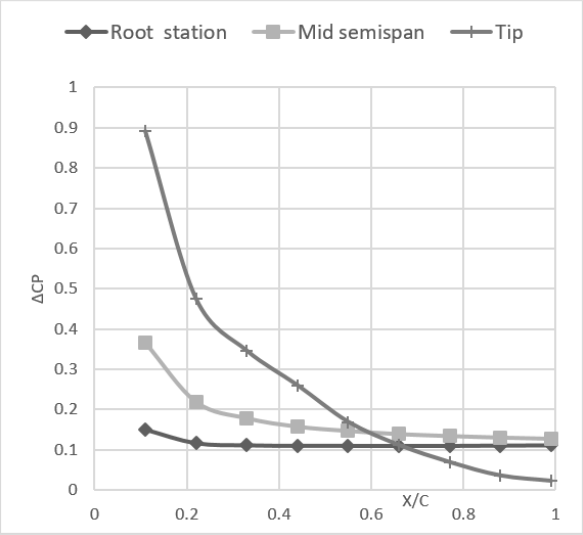

Figure 2. *Chordwise pressure difference coefficient on flat. plate surface, M_∞=1.1, $\alpha=2^0$.*

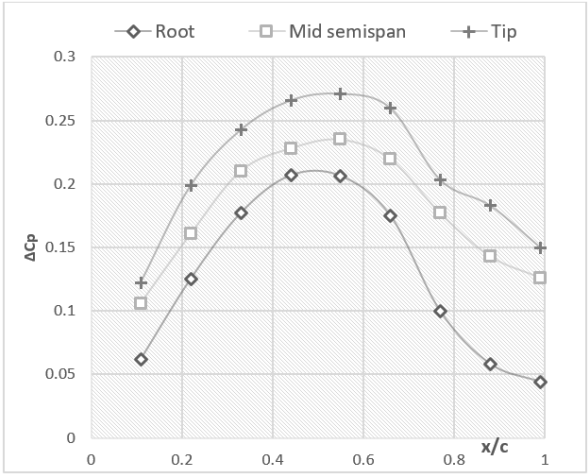

Figure 3. *Constriant-1. Chordwise pressure différence coefficient on optimised profile, M_∞=1.1, $\alpha=2^0$.*

Figures 4, 5, and 6 provide a detailed station-wise comparison of chordwise loading between Constraint 1 and Constraint 3 at the root, mid-semispan, and tip stations, respectively. Enforcing the 10% pitching-moment reduction causes the peak loading to shift forward from approximately 60% of local chord to 40% of local chord. The magnitude of this forward peak is largest at the root station (Figure 4) and diminishes progressively toward the tip (Figure 6). This forward shift is structurally advantageous because high-speed fighter wing main spars are typically positioned near 40% chord, aligning peak aerodynamic load with peak structural stiffness. Simultaneously, the aft loading decreases significantly, creating a crossover point at approximately 60% of local chord across all stations. The trade-off for this forward load concentration is an increase in upper-surface adverse pressure gradients along the mid-chord, which warrants careful off-design assessment.

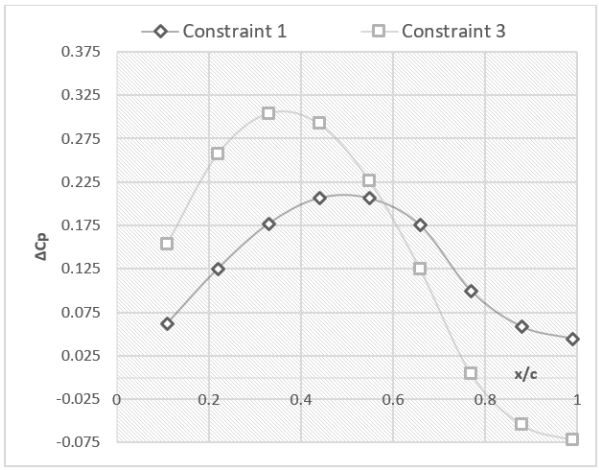

Figure 4. *Loading comparison for root station, M_∞=1.1, $\alpha=2^0$.*

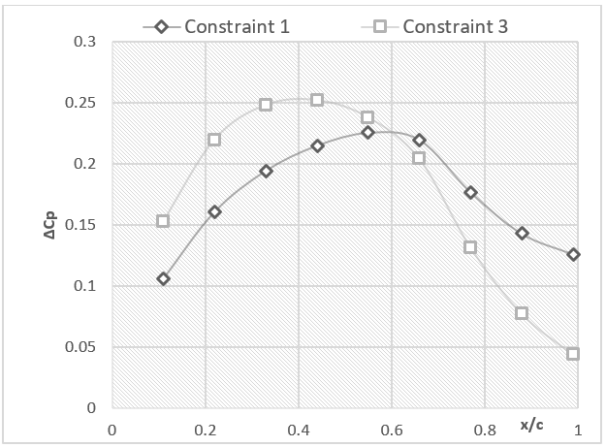

Figure 5. *Loading comparison for mid semispan station, M_∞=1.1, $\alpha=2^0$.*

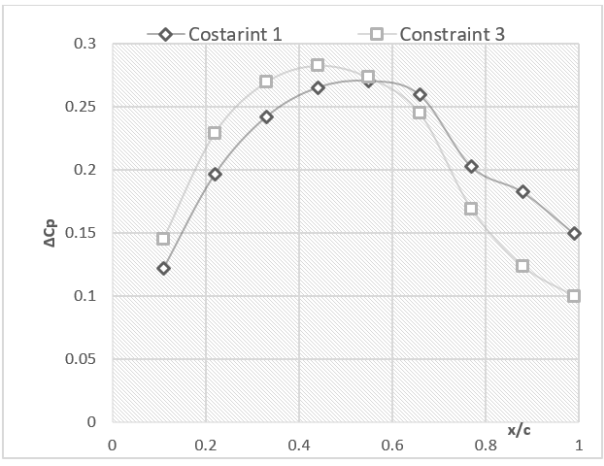

Figure 6. *Loading comparison for tip station, M_∞=1.1, $\alpha=2^0$.*

The spanwise local loading distributions (cCl) for the flat plate, Constraint 1, and Constraint 3 are compared in Figure 7. All three loading distributions intersect at a single invariant pivot point located at approximately 42% of the semispan. For the optimized profiles, local loading increases over the inboard 42% of the span and decreases outboard relative to the flat plate. Under Constraint 3, this inboard load redistribution is even more pronounced, directly contributing to the 3.18% reduction in wing-root bending moment (Table 2) by shifting the spanwise center of pressure inboard.

Figure 8 presents the resulting spanwise aerodynamic twist (washout/wash-in) in radians across the three constraints. The inboard region near the wing root is characterized by wash-in (positive downward incidence). Moving outboard past 30% of the semispan, the warp transitions smoothly into progressive washout that increases continuously toward the tip. This spanwise twist distribution is consistent with classical supersonic camber theories [1, 2], which demonstrate that outboard washout mitigates tip loading and delays compressibility drag rise.

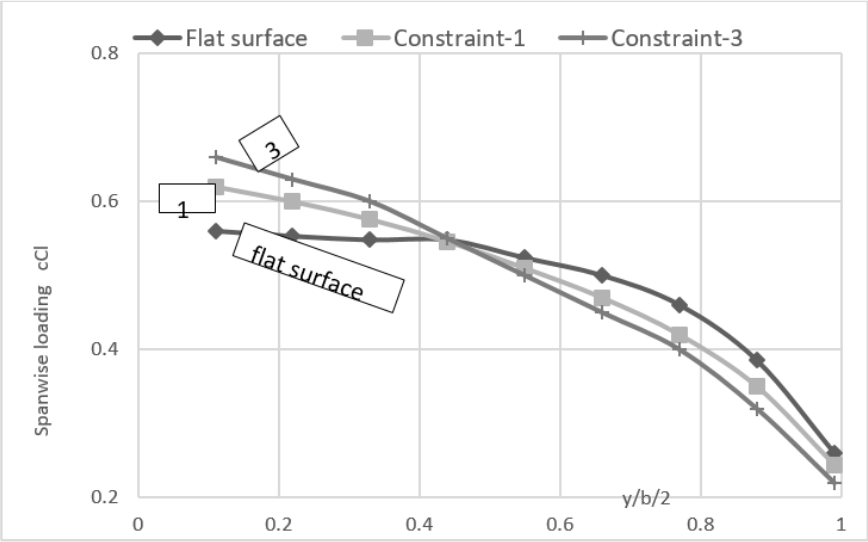

Figure 7. *Spanwise local loading cC_l, $M_\infty=1.1$, $\alpha=2^0$.*

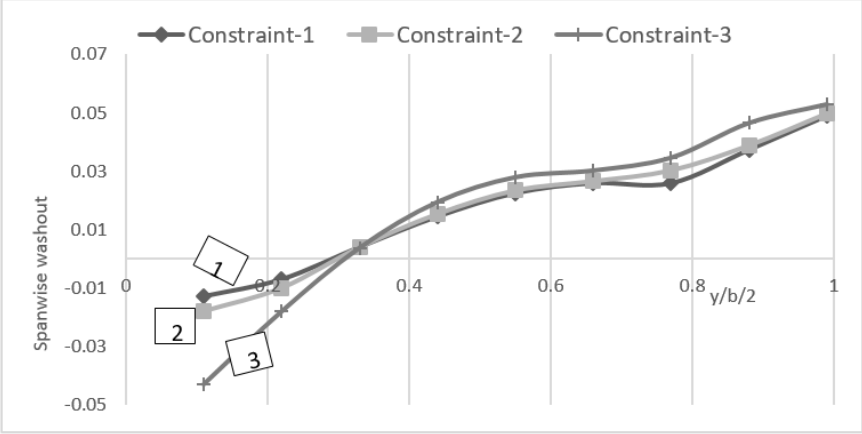

Figure 8. *Spanwise washout in radians, downward values shown positive, $M_\infty=1.1$, $\alpha=2^0$.*

The decoupled chordwise percentage camber distributions are shown in Figures 9 through 14. At the root station (Figure 9), the camber profiles display a distinct reflexed geometry (positive trailing-edge upward curvature). This reflex camber is especially prominent under Constraint 3, demonstrating that the 10% pitching-moment relief is accommodated almost entirely by localized reflex camber at the wing root. In contrast, at the mid-semispan (Figure 10) and tip stations (Figure 11), reflex camber is completely absent; the camber profiles exhibit standard positive curvature that increases monotonically toward the tip. Figures 12, 13, and 14 consolidate these station-wise trends for Constraints 1, 2, and 3, confirming that maximum camber growth occurs across the outboard region.

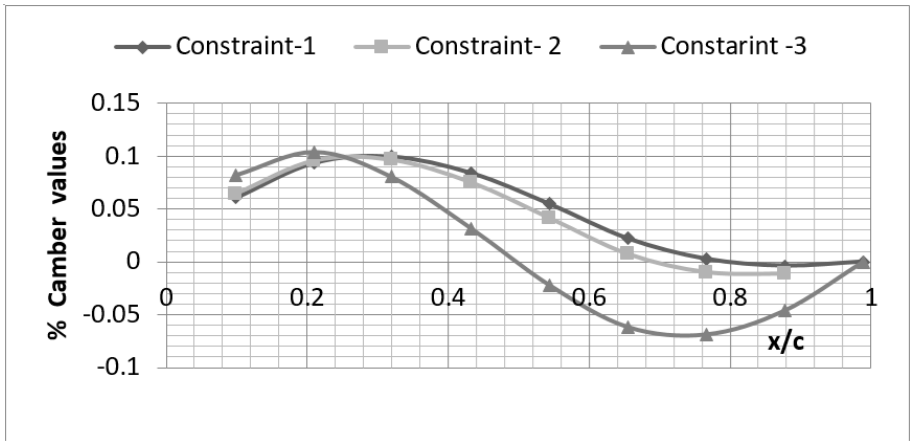

Figure 9. *Chordwise% camber values for all three constraints at root station, M_∞=1.1, $\alpha=2^0$.*

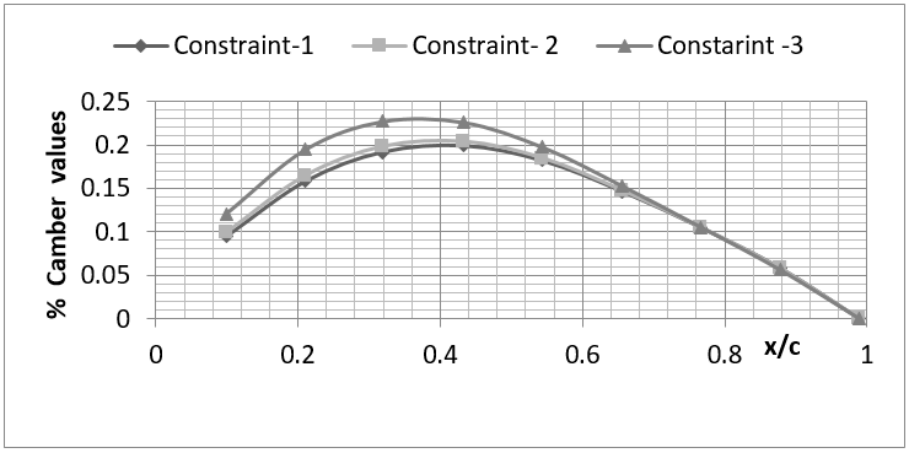

Figure 10. *Chordwise% camber values for all three constraints at mid of semspan, M_∞=1.1, $\alpha=2^0$.*

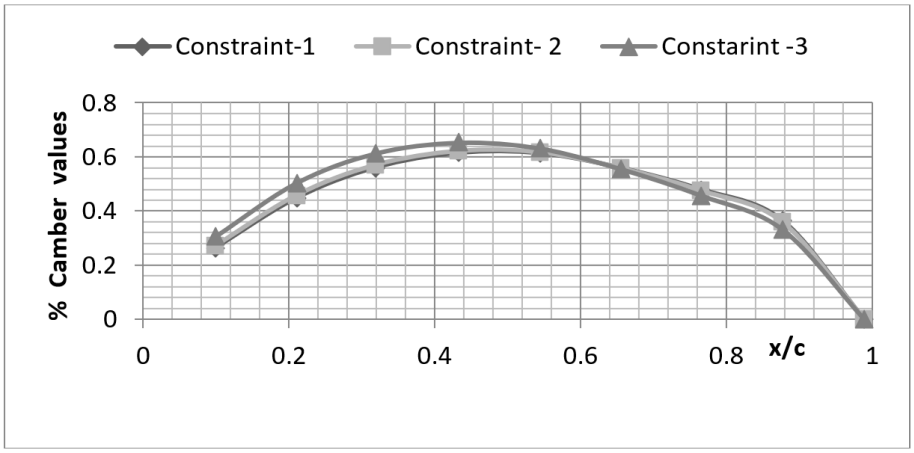

Figure 11. *Chordwise% camber values for all three constraints at tip station, M_∞=1.1, $\alpha=2^0$.*

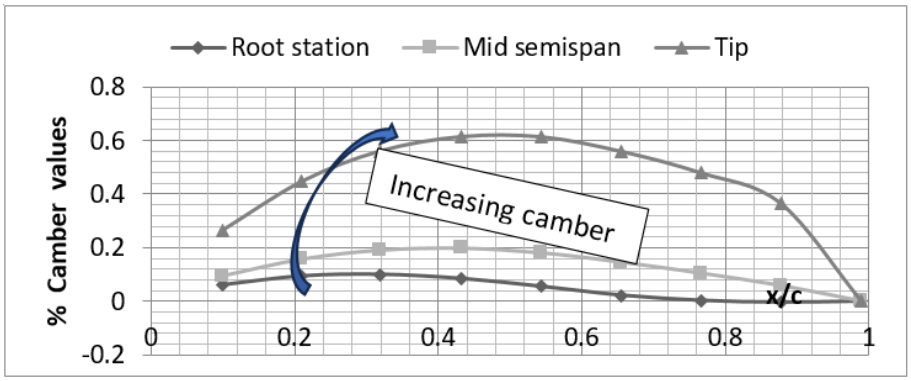

Figure 12. *Constraint -1, Chordwise camber values at three stations. M_{∞}=1.1, α=2⁰.*

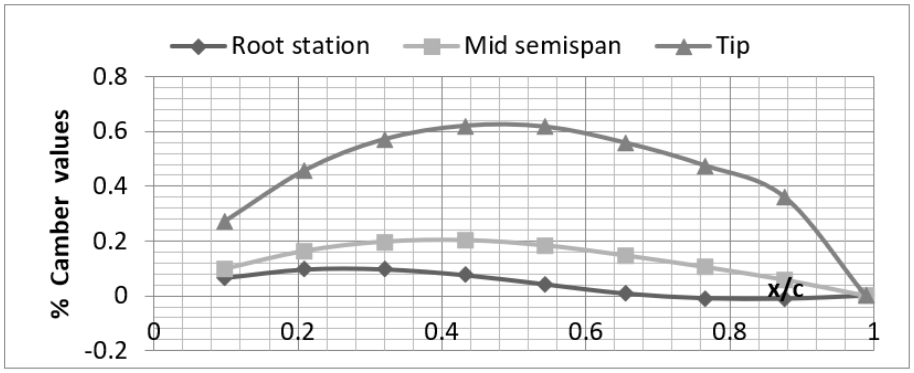

Figure 13. *Constraint -2, Chordwise camber values at three stations, M_{∞}=1.1, α=2⁰.*

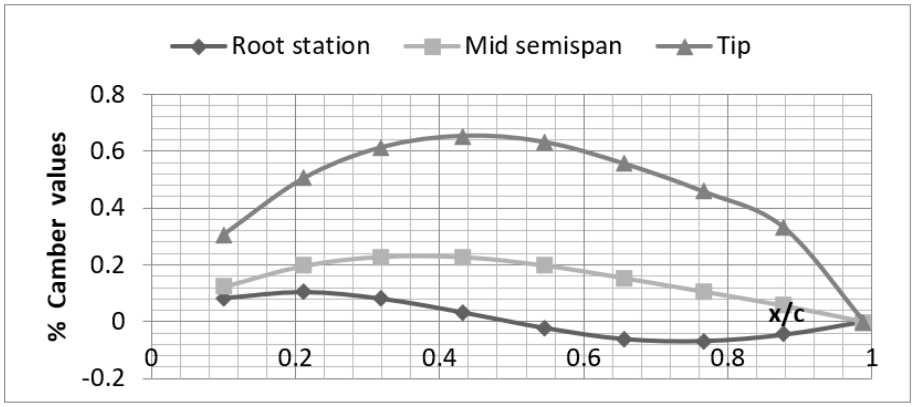

Figure 14. *Constraint -3, Chordwise camber values at three stations, M_{∞}=1.1, α=2⁰.*

The camber slopes generated for Constraints 1 and 3 were superimposed onto a thin NACA 0006 baseline thickness profile to evaluate off-design transonic flow behavior. Figures 15 and 16 depict the upper-surface pressure coefficients at M∞ = 0.95 and α = 0° for the tip and root stations, respectively. The steep pressure recovery (drop in suction) indicates the formation of an upper-surface shock wave. Comparing Figures 15 and 16 reveals that the shock wave is significantly stronger at the tip than at the root, driven by the higher outboard camber and local Mach number acceleration. Figure 17 illustrates the sensitivity of tip surface pressure to freestream Mach number (M∞ = 0.90 to 0.95) under Constraint 3, showing that the compression shock intensifies and moves rearward with increasing Mach number. Figure 18 displays the off-body field values of Cp at the tip station for M∞ = 0.95, confirming that local perturbations decay smoothly into the far field without spurious numerical reflections.

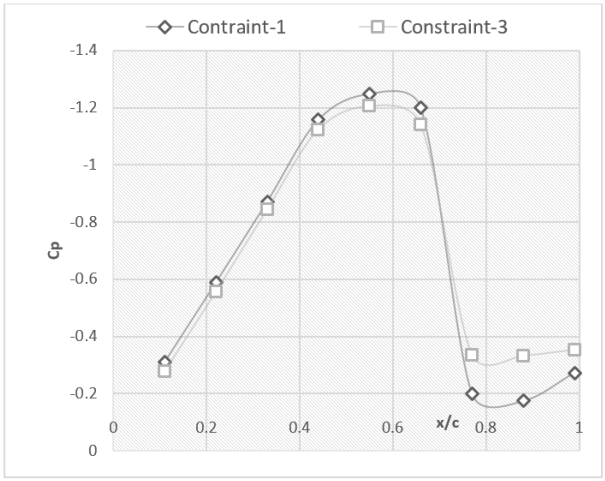

Figure 15. *Upper surface pressure coefficient- Tip station, alpha 0^0, M_∞=0.95.*

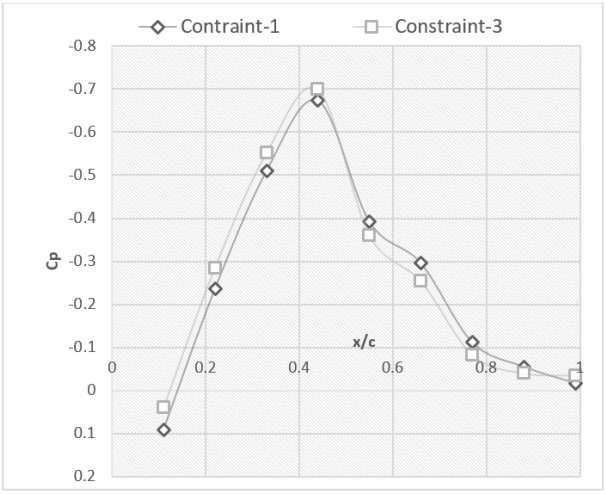

Figure 16. *Upper surface pressure coefficient- Root station, alpha 0^0, M_∞=0.95.*

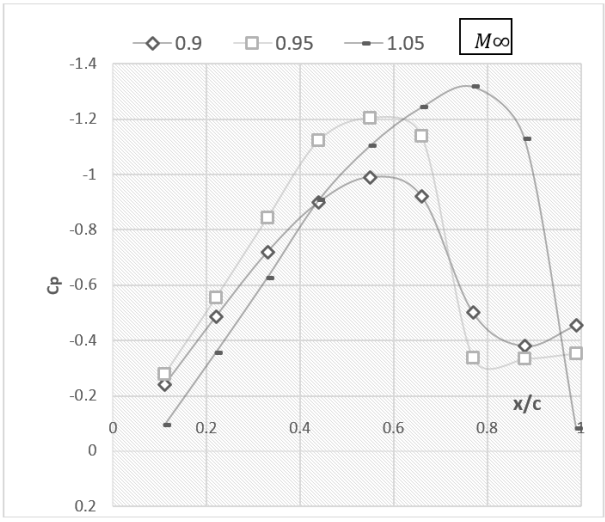

Figure 17. *Upper surface pressure coefficient. Effect of variation in Mach Number-Tip station, alpha=0^0, 3rd Constraint.*

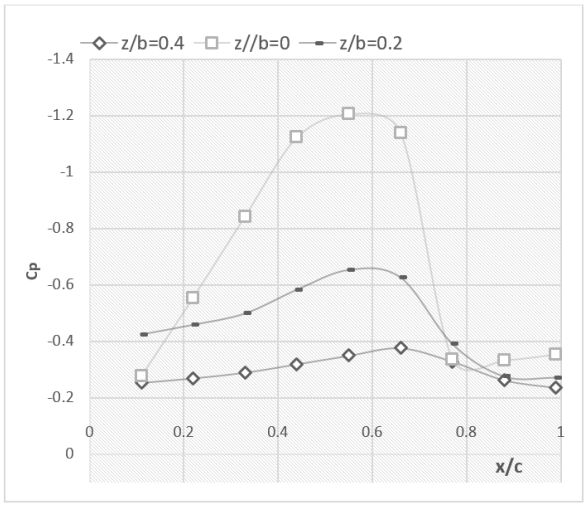

Figure 18. *Upper surface pressure coefficient, 3rd Constraint Tip station, Alpha=0^0, M_∞=0.95, field values.*

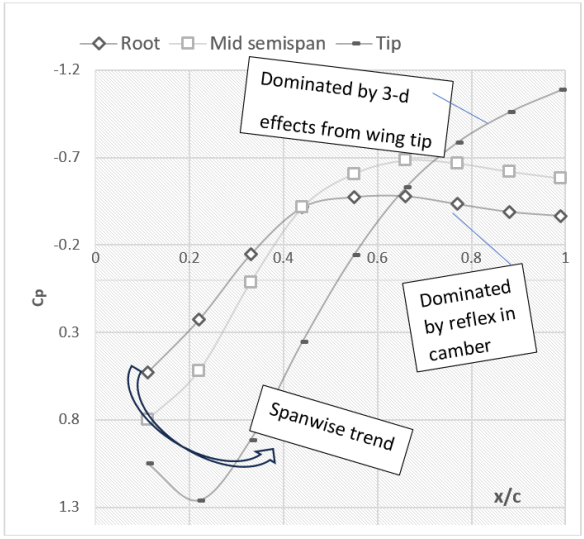

Figure 19. *Spanwise variations of upper surface pressure, 3rd constraint, alpha=4^0, M_∞=1.55.*

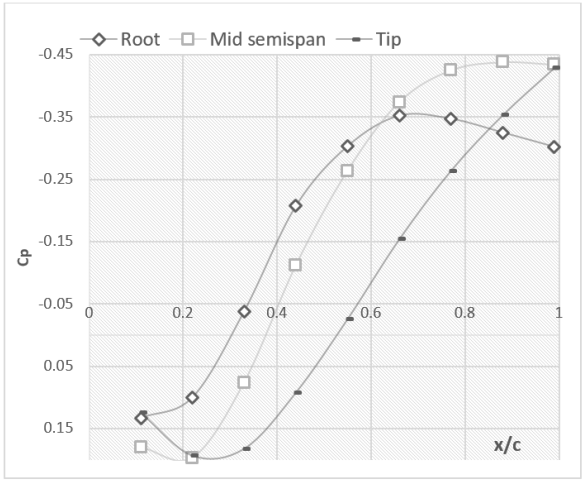

Figure 20. *Spanwise variations of upper surface pressure, 3rd constraint, alpha=4^0, M_∞=2.0.*

To assess off-design behavior at higher supersonic speeds, the Constraint 3 profile was analyzed at M∞ = 1.55 and M∞ = 2.0 at α = 4°. At M∞ = 1.55 (Figure 19), the freestream Mach angle matches the leading-edge sweep (μ = arcsin (1/1.55) = 40.18° vs Λle = 50°), establishing a sonic leading edge that eliminates communication between upper and lower surfaces. Positive pressures dominate the forward wing and increase outboard due to increasing camber, followed by recompression and suction recovery aft. At M∞ = 2.0 (Figure 20), the leading edge becomes fully supersonic. Absolute pressure coefficient levels decrease substantially because narrower upstream Mach cones reduce upstream influence. Both regimes confirm that the reflex-cambered root maintains favorable pressure recovery without flow breakdown.

Physical Scope and Numerical Limitations: The present numerical framework employs an inviscid potential transonic small perturbation formulation. While the Murman-Cole type switching scheme with artificial viscosity accurately captures weak isentropic shock waves (valid for M∞ ≤ 1.1–1.2 where entropy generation scales as O ($(M^2-1)^3$)), it does not resolve viscous boundary-layer thickening, shock-induced boundary-layer separation, or shock-buffet dynamics [16]. Furthermore, while the vortex panel method provides exact induced-drag sensitivities, skin-friction drag and viscous trim penalties require future multi-fidelity RANS or Reynolds-averaged validation.

4. Conclusions

This study investigated the aerodynamic optimization of a low-aspect-ratio supersonic delta wing subject to an explicit pitching-moment constraint, followed by an evaluation of off-design transonic flow behavior using a 3D transonic small perturbation formulation. The primary scientific findings are summarized as follows:

1) Longitudinal Stability Alleviation: Enforcing a 10% pitching-moment reduction under Constraint 3 (0.9$\bar{M}$y) shifts the aerodynamic center forward from 75.4% cr to 66.8% cr on the root chord. This 8.6% forward shift directly mitigates the supersonic Mach tuck phenomenon, alleviating trim drag penalties and restoring pitch control authority.
2) Structural Bending Moment Relief: The moment constraint redistributes spanwise loading inboard across an invariant pivot point at 42% semispan, yielding a 3.18% reduction in wing-root bending moment (Mx*/Mx = 0.9264 vs 0.9569). This reduction provides favorable structural weight savings in high-speed fighter design.
3) Aerodynamic Drag Trade-off: Constraint 3 delivers a 26.30% induced drag reduction relative to the flat plate (CDi = 0.0042 vs 0.0057), achieving a lift-to-induced-drag ratio of 38.74. Accommodating the 10% moment constraint incurs a modest 9.5% drag trade-off relative to the unconstrained-moment optimum (CDi = 0.0038).
4) Localized Reflex Camber Mechanism: Decoupling optimal warp demonstrates that pitching-moment relief is accommodated almost entirely by localized reflex camber at the wing root. Mid-semispan and outboard sections exhibit no reflex, with camber increasing progressively toward the wing tip.
5) Transonic Shock Characteristics: Off-design transonic evaluations (M∞ = 0.90–0.95) reveal upper-surface shock wave formation that intensifies outboard toward the tip. Decoupling warp into spanwise washout and camber ensures stable pressure recovery across both transonic and higher supersonic regimes (M∞ = 1.55 and 2.0).

Abbreviations

TSP	Transonic Small Perturbation
ASO	Aerodynamic Shape Optimisation

Author Contributions

Maddineni Sai Deekshit: Conceptualization, Software
Satish Chander Gupta: Formal Analysis, Methodology

Conflicts of Interest

The authors declare no conflicts of interest.

Appendix: Nomenclature

A = Panel Area
$a_{i,j}$ =Influence of j_{th} panel on i_{th} control point
b = Span
c = local chord
ΔCp =Pressure difference coefficient
C_{Di} =Induced drag coefficient
C_L =Lift coefficient
C_l =Local lift coefficient
C_{mx} =Wing root bending moment coefficient
C_{my} =Pitching moment coefficient about wing apex
C_r =Root chord
C_t =Tip chord
Cp = Pressure coefficient
D = Induced drag
L = Lift
M =Local Mach numbers
M_∞ =Freestream Mach number
M_x =Wing root bending moment about longitudinal axis
M_y =Pitching moment about y axis
N =Number of panels
U =Freestream velocity
u, v, w = Three components of velocities in the x, y, and z directions respectively.

x, y, z = Chordwise, Spanwise and Vertical coordinates respectively

ξ,η,ς = Chordwise, spanwise and vertical coordinates in computational plane

Φ =Velocity potential

ρ =Density

α =Angle-of-Attack (Alpha)

γ = Circulation strength of panels

Λ =leading edge sweep

Suffix

le = Leading edge

te = Trailing edge

N =Number of panels

References

[1] Martins, J. R. R. A. Aerodynamic Design Optimisation: Challenges and Perspectives. Computers & Fluids. 2022, 239, 105391. https://doi.org/10.1016/j.compfluid.2022.105391

[2] Sorrells, R. B., Miller, D. S. Numerical Method for Design of Minimum-Drag Supersonic Wing Camber with Constraints on Pitching Moment and Surface Deformation. NASA Technical Note. 1972, NASA TN D-7097, 1-63.

[3] Gupta, S. C. Development of Algorithms and Computer Codes for Aerodynamic Configuration Design. American Journal of Aerospace Engineering. 2026, 12(1), 1-12. https://doi.org/10.11648/j.ajae.20261201.11

[4] Mader, C. A., Martins, J. R. R. A. Stability-Constrained Aerodynamic Shape Optimization of a Flying Wing Configuration. 13th AIAA/ISSMO Multidisciplinary Analysis and Optimization Conference. 2010, AIAA Paper 2010-9118, 1-17. https://doi.org/10.2514/6.2010-9118

[5] Gupta, S. C. Applied Computational Fluid Dynamics. Wiley India Pvt. Ltd., New Delhi, India. 2019.

[6] Malone, B., Mason, W. H. Multidisciplinary Optimization in Aircraft Design Using Analytic Technology Models. Journal of Aircraft. 1995, 32(2), 431-438. https://doi.org/10.2514/3.46733

[7] Gupta, S. C. A Reconstructive Approach for Design of a Planar Supercritical Wing. Journal of Aerospace Sciences & Technologies. 2021, 73(2), 129-137.

[8] Steger, J. L., Klineberg, J. M. A Finite-Difference Method for Transonic Airfoil Design. AIAA Journal. 1973, 11(5), 628-635. https://doi.org/10.2514/3.6806

[9] Premasuthan, S., Liang, C., Jameson, A. Computation of Flows with Shocks Using Spectral Difference Scheme with Artificial Viscosity. 48th AIAA Aerospace Sciences Meeting Including the New Horizons Forum and Aerospace Exposition. 2010, AIAA Paper 2010-1449, 1-15. https://doi.org/10.2514/6.2010-1449

[10] Murman, E. M., Cole, J. D. Calculation of Plane Steady Transonic Flows. AIAA Journal. 1971, 9(1), 114-121. https://doi.org/10.2514/3.6134

[11] Jameson, A. Iterative Solution of Transonic Flows Over Airfoils and Wings, Including Flows at Mach 1. Communications on Pure and Applied Mathematics. 1974, 27(3), 283-309. https://doi.org/10.1002/cpa.3160270304

[12] Carlson, H. W., Miller, D. S. Numerical Methods for the Design and Analysis of Wings at Supersonic Speeds. NASA Technical Note. 1974, NASA TN D-7713, 1-76.

[13] Serani, A., Diez, M., Quagliarella, D. Aerodynamic Shape Optimization in Transonic Conditions Through Parametric Model Embedding. Aerospace Science and Technology. 2024, 155, 109611. https://doi.org/10.1016/j.ast.2024.109611

[14] Seraj, S., Yildirim, A., Martins, J. R. R. A. Aerodynamic Shape Optimization of a Supersonic Transport Including a Subsonic Static Margin Constraint. Aerospace Science and Technology. 2025, 166, 110565. https://doi.org/10.1016/j.ast.2025.110565

[15] Chau, T., Zingg, D. W. Aerodynamic Optimization and Fuel Burn Evaluation of a Transonic Strut-Braced-Wing Single-Aisle Aircraft. Journal of Aircraft. 2023, 60(5), 1638-1658. https://doi.org/10.2514/1.C037158

[16] Petrocchi, A., Mauriello, M., Barakos, G. Transonic Buffet Alleviation via Virtual Control Surfaces. Aerospace Science and Technology. 2023, 140, 108478. https://doi.org/10.1016/j.ast.2023.108478

[17] Pang, B., Zhang, Y., Li, J., Wang, X., Ma, C., Bai, J. Data-Driven Surrogate Model for Aerodynamic Design Using Separable Shape Tensor Method. Chinese Journal of Aeronautics. 2024, 37(9), 41-58. https://doi.org/10.1016/j.cja.2024.03.014

[18] Sudhi, A., Radespiel, R., Badrya, C. Design Exploration of Transonic Airfoils for Natural and Hybrid Laminar Flow Control Applications. Journal of Aircraft. 2023, 60(3), 716-732. https://doi.org/10.2514/1.C036968